Geoscientific
Model Development
Discussions

Open Access

EGU

1

1 **Improving Madden–Julian Oscillation Simulation in Atmospheric General**

2 **Circulation Models by Coupling with Snow–Ice–Thermocline One-dimensional**

3 **Ocean Model**

4 Wan-Ling Tseng[1], Huang-Hsiung Hsu[1*], Yung-Yao Lan[1], Chia-Ying Tu[1], Pei-Hsuan

5 Kuo[2], Ben-Jei Tsuang[3], Hsin-Chien Liang[1]

6

7 [1]Research Center for Environmental Changes, Academia Sinica, Taipei, Taiwan

8 [2]Center Weather Bureau, Taipei, Taiwan.

9 [3]National Chung-Hsing University, Taichung, Taiwan.

10 Corresponding author: Huang-Hsiung Hsu (hhhsu@gate.sinica.edu.tw)

11

Geoscientific
Model Development
Discussions

12 **Abstract**

13   A one-column turbulent kinetic energy–type ocean mixed-layer model Snow–Ice–

14 Thermocline (SIT) when coupled with three atmospheric general circulation models

15 (AGCMs) to yielded superior Madden–Julian Oscillation (MJO) simulation. SIT is

16 designed to have fine layers similar to those observed near the ocean surface and therefore

17 can realistically simulate the diurnal warm layer and cool skin. This refined discretization

18 of the near ocean surface in SIT provides accurate sea surface temperature (SST)

19 simulation, thus facilitating realistic air–sea interaction. Coupling SIT with European

20 Centre Hamburg Model, Version 5 (ECHAM5); Community Atmosphere Model, Version

21 5 (CAM5); and High Resolution Atmospheric Model (HiRAM) significantly improved

22 MJO simulation in three coupled AGCMs compared with the AGCM driven with

23 prescribed SST. This study suggests two major improvements to the coupling process.

24 First, during the preconditioning phase of MJO over Maritime Continent (MC), the over

25 underestimated surface latent heat bias in AGCMs can be corrected. Second, during the

26 phase of strongest convection over MC, the change of the intraseasonal circulation in the

27 meridional circulation is the dominant factor in the coupled simulations relative to the

28 uncoupled experiments. The study results indicate that a fine vertical resolution near the

29 surface, which better captures temperature variations in the upper few meters of the ocean,

30 considerably improves different models with different configurations and physical

31 parameterization schemes; this could be an essential factor for accurate MJO simulation.

32 **Keywords:** Madden–Julian Oscillation, coupling, warm layer

33

34 **Short summary (plain text)**

35   We show that coupling a high-resolution one-column ocean model to three

36 atmospheric general circulation models dramatically improves Madden–Julian oscillation

37 (MJO) simulations. It suggests two major improvements to the coupling process in

38 preconditioning phase and strongest convection phase over Maritime Continent. Our

39 results demonstrate a simple but effective way to significantly improve MJO simulation

40 and potentially also seasonal to subseasonal prediction.

41

42

1 Introduction

43

44   The Madden–Julian Oscillation (MJO) is the dominant pattern of atmospheric

45   intraseasonal variability in the tropics (Madden and Julian 1972; Zhang 2005; Jiang et al.

46   2020). It has been reported that the MJO convection is most often observed over sea

47   surface temperature (SST) of >28°C in the Indo-Pacific warm pool (Salby and Hendon

48   1994). The MJO is an eastward-propagating ocean–atmosphere and convection–

49   circulation coupled phenomenon that lasts for 20–100 days. On these timescales, low-

50   level moisture convergence, warm SST, and shallow upper-ocean mixed-layer depth

51   precede the eastward propagation of organized deep convection by approximately 10 days;

52   opposite conditions follow by approximately 10 days (Krishnamurti et al. 1988; Hendon

53   and Salby 1994; Woolnough et al. 2000). Heat flux exchange between the atmosphere

54   and ocean modulates the intraseasonal oscillation (Shinoda and Hendon 1998; Shinoda et

55   al. 1998). Studies have emphasized the importance of moisture and heat flux feedback in

56   MJO (Sobel et al. 2008, 2010; DeMott et al. 2015). Besides, the MJO and oceanic wave

57   dynamics are also suggested such as zonal wind stress anomalies associated with the MJO

58   force eastward-propagating oceanic equatorial Kelvin wave (Hendon et al. 1998; Webber

59   et al. 2010), and the signals could extend as deep as 1500 m in the ocean (Matthews et al.

60   2007). Furthermore, the westward-propagating oceanic equatorial Rossby wave can

61   initiate the next MJO in the Indian Ocean (Webber et al. 2010; Webber et al. 2012).

62   Evidence of oceanic intraseasonal signals coupling with atmospheric signals was

63   observed in terms of the sea level, surface heat flux, salinity, and temperature during field

64   experiments and in situ monitoring (Oliver and Thompson 2011; Drushka et al. 2012;

65   Wang et al. 2013; Chi et al. 2014; DeMott et al. 2015; Fu et al. 2015).

66   Recent modeling studies evaluating the mechanism of ocean–atmosphere coupling

67   have indicated that most coupled models could improve MJO simulations but that the

68   ocean driven by the atmosphere contributes indirectly through improvement in the mean

69   state, heat flux, fresh water, and momentum. DeMott et al. (2016) estimated that direct

70   SST-driven ocean feedback contributes MJO propagation up to 10% by change in column

71   moisture. A comparison of the direct and indirect effects of SST indicated that direct

72   effects such as SST-driven surface fluxes tend to offset wind-driven fluxes (DeMott et al.

73   2015; DeMott et al. 2016; DeMott et al. 2019). The key factor of indirect ocean feedback

74   in the atmospheric physical process, such as strong MJO convection can amplify the

75   radiative feedback to MJO convections associated with large cloud system (Del Genio

76   and Chen 2015), the SST gradients can dive the MJO low-level convergence (Hsu and Li

77   2012; Li and Carbone 2012), or destabilize lower tropospheric enhance low-level

78   convergence to east of MJO convergence (Wang and Xie 1998; Marshall et al. 2008;

79   Benedict and Randall 2011; Fu et al. 2015). Many observational and model studies have

80   reported that coupled feedback enhances the MJO with strong horizontal moisture

81   advection, driven by sharp mean near-equatorial meridional moisture gradients (DeMott

82   et al. 2015; Jiang et al. 2018; DeMott et al. 2019; Jiang et al. 2020). These finding suggest

83   that high-frequency SST perturbations could improve moisture convergence efficiency

84   and enhance MJO propagation through relatively smooth background moisture

85   distribution.

86   Tseng et al. (2015) identified the key role of the upper-ocean warm layer in

87   improving the MJO eastward propagation simulation by using the European Centre

88   Hamburg Model, Version 5 (ECHAM5), coupled with the one-column ocean model

89   named Snow–Ice–Thermocline (SIT). Many observational (Drushka et al. 2012; Chi et

90 al. 2014) and modeling (Klingaman and Woolnough 2013; DeMott et al. 2019;

91 Klingaman and Demott 2020) studies have supported this hypothesis. However, coupling

92 the SIT to only one atmospheric general circulation model (AGCM) may be insufficient

93 to prove the effect of the coupling. In the current study, we coupled the SIT to three

94 AGCMs: European Centre Hamburg Model, Version 5 (ECHAM5); Community

95 Atmosphere Model, Version 5 (CAM5); and High Resolution Atmospheric Model

96 (HiRAM). As well as one additional high-resolution forecast model from Central Weather

97 Bureau, Taiwan (CWBGFS) to demonstrate that the improvement of MJO simulation

98 through coupling the upper-ocean warm layer is AGCM independent. Furthermore, we

99 discussed the coupling mechanism that leads to simulation improvement. Models, the

100 experimental design, and observational data are described in Section 2. Section 3 presents

101 the results, followed by a discussion in Section 4.

102 **2 Models, experiments, and observational data**

103   Observational data used in this study include precipitation from Global Precipitation

104 Climatology Project V1.3 (GPCP, 1° resolution) (Adler et al. (2003), outgoing longwave

105 radiation (OLR, 1° resolution) (Liebmann (1996)), and daily SST (Optimum Interpolated

106 SST, 0.25° resolution) (Banzon et al. (2014)) from the National Oceanic and Atmosphere

107 Administration, and variables were obtained from the European Centre for Medium-range

108 Weather Forecast Reanalysis-interim (Dee et al. 2011). We used a 22-year ERA-Interim

109 from 1989 to 2010 and a 14-year GPCP dataset from 1997 to 2010. Oceanic observational

110 data include those from the NCEP Global Ocean Data Assimilation System (GODAS)

111 (Behringer and Xue (2004) provided by the NOAA/OAR/ESRL PSL, Boulder, Colorado,

112   USA (https://psl.noaa.gov/data/gridded/data.godas.html) and in situ temperature profiles

113   from the Tropical Ocean Global Atmosphere program (McPhaden et al. 2010).

114   In this study, we coupled the SIT one-column ocean model (Tu and Tsuang 2005;

115   Tsuang et al. 2009) to four AGCMs. SIT simulates variations in the SST and upper-ocean

116   temperature, including the diurnally varying cool skin and warm layer in the upper few

117   meters of the ocean and the turbulent kinetic energy (TKE) (Gaspar et al. (1990)) in the

118   water column (Tu and Tsuang 2005; Tsuang et al. 2009; Tseng et al. 2015). The four

119   AGCMs used here are as follows. (1) ECHAM5, a the fifth-generation AGCM developed

120   at the Max Planck Institute for Meteorology (Roeckner 2003; Roeckner et al. 2006). It is

121   a spectral model employing the Nordeng (Nordeng 1994) cumulus convective scheme.

122   We used a horizontal resolution of T63 (approximately 2°) with 31 vertical layers and a

123   model top at 10 hPa (approximately 30 km). (2) NCAR CAM5 in Community Earth

124   System Model, version 1.2.2 (Hurrell et al. 2013) from the National Center for

125   Atmospheric Research. (3) HiRAM, developed based on Geophysical Fluid Dynamical

126   Laboratory global atmosphere and land model AM2 (Team et al. 2004; Zhao et al. 2009)

127   with few modifications (Chen et al. 2019). We also used CWBGFS, the second-

128   generation global forecast system at the Central Weather Bureau in Taiwan (Liou et al.

129   1997), which employs the cumulus convective scheme of Nordeng (1994), shallow

130   convective scheme of (Li and Wang 2000), and boundary layer of Hong and Pan (1996).

131   In this study, we applied 42 vertical layers in SIT, with 12 layers in the upper 10 m.

132   In the upper 10 m, fine resolution was designed to realistically simulate the upper-ocean

133   warm layer, including a layer at 0.05 mm, reproducing the cool skin of the ocean surface.

134   Notably, coupling of a high-vertical-resolution TKE ocean model with an AGCM is

135   unconventional. To account for neglected horizontal processes, the model ocean was

8

136   weakly nudged (with a 30-day time scale) to the observed GODAS monthly mean ocean

137   temperature below a depth of 10 m. Nudging was not applied in the upper 10 m. The SIT

138   and AGCMs exchange ocean surface fluxes at every time step 48 times a day. AGCMs

139   were coupled with the SIT in the tropical region between 30°S and 30°N and forced by

140   prescribed climatological monthly mean SST.

141   The experiments included three sets of coupled AGCM simulations (ECHAM5-SIT,

142   CAM5-SIT, and HiRAM-SIT) and standalone AGCM simulations forced by observed

143   monthly mean OISST (ECHAM5, CAM5, and HiRAM) from 1985 to 2005. The

144   experiments were designed to evaluate the effect of atmosphere–ocean coupling on MJO

145   simulations. Table 1 presents the model and experiment details. Due to the computation

146   limitation of a high-resolution forecast model, the CWBGFS-SIT was only run for 3 years

147   to test the coupling effect. Thus, its results were evaluated but not compared with those

148   of the other three models.

149   The analysis focused on the boreal cool season (November–April) when the

150   eastward propagation tendency of the MJO is the most prominent. We used the CLIVAR

151   MJO Working Group diagnostics package (CLIVAR 2009) and a 20–100-day filter to

152   analyze intraseasonal variability. The MJO phase composites were computed using the

153   real-time multivariate MJO index (Wheeler and Hendon 2004), which is defined as the

154   leading pair of principal components of intraseasonal OLR, and 850 and 200 hPa zonal

155   winds in the tropics.

156   The vertically integrated MSE budget was diagnosed based on the following

157   equation:

158
$$\langle\frac{\partial h}{\partial t}\rangle' = -\langle u\frac{\partial h}{\partial x}\rangle' - \langle v\frac{\partial h}{\partial y}\rangle' - \langle\omega\frac{\partial h}{\partial p}\rangle' + \langle LW\rangle' + \langle SW\rangle' + \langle LH\rangle' + \langle SH\rangle' \qquad (1)$$

159   where h is the MSE ($h = c_pT + gz + Lq$); u and v are the zonal and meridional velocities,

160   respectively; ω is the vertical pressure velocity; LW and SW are the longwave and

161   shortwave radiation fluxes, respectively; and LH and SH are the latent and sensible

162   surface heat fluxes, respectively. The mass-weighted vertical integration from the surface

163   to 200 hPa is denoted as $\langle \cdot \rangle$, and intraseasonal anomalies are represented as $\langle \cdot \rangle'$. All fields

164   were isolated using a 20–100-day bandpass Lanczos filter (Duchon 1979).

165

166   **3 Results**

167   **3.1 MJO simulations: ECHAM5-SIT, CAM5-SIT, and HiRAM-SIT**

168   **3.1.1 General structure**

169   We compared simulated MJO characteristics using three coupled and uncoupled

170   AGCMs. Figure 1 presents the wavenumber–frequency spectra of simulated 850 hPa

171   zonal wind (shading) and precipitation (contours). All three uncoupled AGCMs (hereafter

172   referred to as AGCMs) simulated intraseasonal signals with lower frequency than the

173   observed and overestimated the westward propagation with periods >80 days (Fig. 1e–g).

174   ECHAM5 and HiRAM simulated signals of wavenumbers 1–3 instead of the observed

175   wavenumber 1 in 850 hPa zonal wind. These results indicate that all three AGCMs

176   simulated stationary fluctuations with low frequency that were not consistent with the

177   observation. By contrast, coupled AGCMs realistically reproduce the observed spectral

178   characteristics and strength of the eastward propagation at wavenumbers 1 to 2 in 850-

179   hPa zonal wind (Fig. 1b–d). Although HiRAM simulated eastward propagation in a wider

180   frequency spectrum than that observed, the coupled model clearly displays improvements

Geoscientific
Model Development
Discussions

181   in the MJO simulation compared with the stationary intraseasonal fluctuation in the

182   uncoupled simulation. Hovmöller diagrams presented in Fig. 2 illustrate the temporal

183   evolution of 850 hPa zonal wind and precipitation in the tropics in observation and

184   simulations. All three models simulated either stationary (CAM5 and HiRAM) or weak

185   eastward-propagating (ECHAM5) signals in AGCMs, but more realistically simulated

186   the eastward propagation of the MJO coupled AGCMs, although the propagation in the

187   ECHAM5-SIT is still slightly slower than that observed. The improvement obtained in

188   coupled models suggests that active ocean–atmosphere interaction is a crucial factor for

189   the successful simulation of the MJO.

190   **3.1.2 Atmospheric and oceanic profiles**

191   The composite MJO life cycle featuring intraseasonal OLR and 10-m surface wind

192   anomalies for boreal winter in eight phases following Wheeler and Hendon (2004) is

193   displayed in Fig. S1–S3. All three coupled AGCMs simulated realistic MJO with

194   enhanced circulations and propagation tendency compared with the uncoupled AGCMs.

195   Figure 3 shows the temporal evolution of vertical heating profiles (averaged over 10°S–

196   EQ, 120°E–150°E) in eight MJO phases. Observed heating profiles, calculated following

197   the definition of the apparent heat source (Q1) (Yanai et al. 1973), exhibit diabatic heating

198   with a maximum near 500 hPa in phases 4 and 5 and in the lower troposphere in earlier

199   phases. This reflects the development from shallow to deep heating during the

200   development stage of the convective phase in an MJO. Both ECHAM and HiRAM exhibit

201   stronger heating in coupled simulations than in uncoupled simulations, whereas the

202   difference is not evident in CAM5. The vertical structures of the apparent moisture sink

203   (Q2; contours) associated with the MJO demonstrate a similar convection development.

11

204   MJO analysis in phase 4 when deep convection is the strongest over the Maritime

205   Continent demonstrates the large-scale zonally overturning circulation coupling with the

206   convection (Fig. 4). The positive heating region in the coupled experiment is significantly

207   enlarged, deepened, and westward-tilted with increasing height compared with those in

208   the uncoupled experiment. Correspondingly, the convective-circulation envelope of the

209   MJO is thicker and longitudinally wider in coupled experiments. The strong convection

210   is associated with much enhanced low-level moisture convergence (green contours).

211   Furthermore, the area of positive rainfall anomaly in the coupled experiment becomes

212   larger, and the sea level pressure anomaly is meridionally more confined, exhibiting the

213   characteristics of intensified Kelvin wave-like perturbations to the east of the deep

214   convection. This enhancement of low-level moisture convergence is consistent with the

215   frictional wave–conditional instability of the second kind mechanism (Wang and Rui

216   1990; Kang et al. 2013).

217   In addition to the atmospheric structure, the SST (Fig. S4) and vertical profile of

218   ocean temperature (Fig. S5) examined are presented in Fig. S5. The observed SST

219   variation in MJO variability is well reproduced in all three coupled models (Fig. S4). The

220   warm SST leads the main MJO convection by approximately 5–10 days and is followed

221   by the cold SST approximately 5–10 days later (Flatau et al. 1997; DeMott et al. 2015;

222   Tseng et al. 2015). Moreover, the observed amplitude fluctuation (approximately 0.5° to

223   1°) is realistically simulated. Observed ocean temperature profiles, characterized by the

224   warm layer, along the equator from the Indian Ocean to the western Pacific are well

225   simulated in the three coupled models (Fig. S5). Simulated temperature anomalies are

226   larger in ECHAM5-SIT than in CAM5-SIT and HiRAM-SIT. These results consistently

227   obtained in all three coupled models support the conclusion of Tseng et al. (2015) that

228   resolving fine vertical resolution in the upper ocean improves the simulation of warm

229   layer and MJO propagation and variability. The effect of atmosphere–ocean coupling on

230   the MJO is independent of AGCMs with different configurations and atmospheric

231   physical parameterizations. Modifying atmospheric physical parameterizations has been

232   shown to improve MJO simulation to some extent (Wang et al. 2021), and the results

233   could be model dependent. Our results demonstrate that the impact of atmosphere–ocean

234   coupling independent of physical schemes seems to be a more fundamental approach.

235   **3.1.3 Performance comparison**

236   To summarize improvements resulting from coupling, simulation was evaluated

237   (Fig. 5). Figure 5a presents the scatter plot of the power ratio of east–west propagating

238   waves (X-axis) versus the pattern correlation between the simulated and observed

239   precipitation anomaly in Hovmöller diagrams (Fig. 2) (Y-axis). The east:west ratio was

240   calculated by dividing eastward-propagating power by westward-propagating power of

241   850 hPa zonal wind summed over wavenumbers 1–2 and a period of 30–80 days.

242   Compared with the observation, coupled simulations (marked by circles) exhibit better

243   simulation than uncoupled simulations (marked by asterisks). A comparison of combined

244   explained variance by using RMM1 and RMM2 (Fig. 5b) based on Wheeler and Hendon

245   (2004) shows marked increases after coupling. A comparison of the coupled and

246   uncoupled simulations demonstrates that coupling is an essential factor for realistic MJO

247   simulations.

248   **3.2 Mechanism discussion**

249   Here, the MSE budget was applied to diagnose the moisture budget associated with

250   the MJO. Figure 6 presents a Hovmöller diagram of MSE tendency averaged by 10°S–

Geoscientific
Model Development
Discussions

251   EQ overlaying precipitation anomalies. MSE tendency changes in quadrature with

252   precipitation anomaly with positive (negative) MSE tendency, leading (lagging) major

253   convection by approximately one to two phases (DeMott et al. 2015; DeMott et al. 2016;

254   DeMott et al. 2019). Coupled models simulate stronger eastward propagation in both

255   MSE tendency and precipitation anomalies. Stronger MSE tendencies in coupled

256   simulations are seen in ECHAM5 and HiRAM but are less clear in CAM5. The

257   differences between coupled and uncoupled simulations are presented in Fig. 6d, g, j. One

258   notable feature is the positive (negative) MSE tendency preceding positive (negative)

259   precipitation anomaly and preconditions an environment for eastward propagation of

260   active (inactive) convection and associated circulation. We diagnosed the relative

261   contribution of each term in Equation 1 to the MSE tendency with the focus on the MC,

262   where the largest positive MSE tendency and precipitation anomaly were found.

263   **3.2.1 Preconditioning phase**

264   Following the peak MSE tendency over the MC (120°E–150°E) during phase 2 (Fig.

265   6d, g, j), values of each term contributing to the column-integrated MSE tendency in

266   Equation 1 during phase 2 preceding the deep convection over the MC area (10°S–EQ,

267   120°E–150°E) are displayed in Fig. 7. Vertical advection is the dominant term with the

268   major compensation from long-wave radiation during phase 2 when convection is still in

269   the eastern Indian Ocean, as identified by Wang et al. (2017). However, this effect is not

270   better simulated in the coupled experiments than in the uncoupled experiments in all three

271   models. Notably, the LH term is consistent between both phases. In all three models, the

272   coupling reduces the negative MSE tendency. The results indicate that the contribution

273   comes for the LH in this early phase stage. The LH effect was overlooked in Tseng et al.

Geoscientific
Model Development
Discussions

274 (2015) because of the weak MJO variability in coupled simulations. However, this

275 smaller LH negative became one of the key factors in enhancing the leading MSE

276 tendency during the MJO preconditioning phases. This suggests that by involving the

277 coupling process in the preconditioning phase, the surface latent flux bias in AGCMs can

278 be corrected. In general, coupling improves the simulation of budget. The positive

279 contribution of vertical advection and negative contribution of LH in MSE tendency is

280 closer to realistic in the coupled simulations during the initial phase of the MJO.

281 **3.2.2 Phase of strongest convection over MC**

282 We compared the spatial distribution of MSE and precipitation in phase 4 when

283 convection was the strongest in the MC (Fig. 8). In the observation, the main convection

284 occurs in the MC from 90°E to 150°E. A positive MSE tendency with a maximum near

285 10°N and 10°S is identified in the east of the MJO convection centered near the equator.

286 Conversely, a negative integrated MSE tendency is found in the west of the MJO

287 convection, and the meridionally confined structure near the equator seems to exhibit the

288 characteristics of the equatorial Kelvin wave embedded in the MJO. Clearly, coupled

289 models outperform uncoupled models in reproducing these signals. To quantify the

290 contribution of coupling to the improvement, we follow Jiang et al. (2018) to project all

291 MSE terms to the observations (Fig. 9). The dominant contribution of horizontal

292 advection to the MSE tendency in observation (Fig. 9a) is well simulated in the coupled

293 simulations but not in uncoupled simulations by ECHAM5 and CAM5 (Fig. 9b, c).

294 Although a similar dominant effect is noted in both simulation types in HiRAM, it is more

295 enhanced in the coupled simulation (Fig. 9d). The horizontal advection term is further

296 decomposed into zonal and meridional components (Fig. 9e–h); both components have a

297 positive contribution, but the meridional component has a larger amplitude. Uncoupled

298 ECHAM5 and CAM5 simulate unrealistic features: positive contribution from zonal

299   advection but negative contribution from meridional advection. By contrast, coupled

300   models well simulate the dominance of meridional advection. In HiRAM, the uncoupled

301   model simulates almost equally positive contributions from both terms, but the coupled

302   model is able to simulate the larger contribution from meridional advection. We further

303   decompose the meridional advection to assess the relative contributions of intraseasonal

304   perturbation and the mean state. Consistent with the observations (Fig. 9i), the meridional

305   advection by intraseasonal flow $(-v' \frac{\partial \bar{h}}{\partial y})$ is the main contribution to improve the

306   simulations in the coupled models (Fig. 9j–l). Our results are consistent with those of

307   Jiang et al. (2018). To evaluate the relative contribution of intraseasonal circulation and

308   background moisture, changes in $\Delta(-v' \frac{\partial \bar{h}}{\partial y})$ at phase 4 were further diagnosed. Overbar

309   denotes that the time mean and prime represents intraseasonal anomaly. Changes in the

310   MJO meridional advection term for coupled experiments relative to uncoupled can be

311   written as follows:

312    $$\Delta\left(-v'\frac{\partial \bar{m}}{\partial y}\right) = -\Delta v' \left(\frac{\partial \bar{m}}{\partial y}\right)_{uncoupled} - (v')_{uncoupled} \Delta\left(\frac{\partial \bar{m}}{\partial y}\right) - \Delta v' \Delta\left(\frac{\partial \bar{m}}{\partial y}\right) \quad (2)$$

313   (a) (b) (c)

314   where Δ represents the coupled–uncoupled change. The terms a–c are presented as bar

315   charts in Fig. 10. Notably, the change of the intraseasonal circulation in the meridional

316   circulation is the dominant factor in coupled simulations relative to uncoupled

317   experiments. The results confirm that the dominance of dynamic influence over

318   thermodynamic response to atmosphere–ocean coupling is the key process leading to an

319   improvement in MJO simulations.

320

321   **3.3 Discussion: mean state and intraseasonal variance**

322   We examined the simulated mean state, which is a major issue affecting MJO

323   simulations (Inness et al. 2003; Watterson and Syktus 2007; Kim et al. 2009; Kim et al.

324   2011; Kim et al. 2014; Jiang et al. 2018; Jiang et al. 2020). The three models exhibited

325   different tropical SST responses to coupling (Fig. S6e). Over the warm pool area, both

326   CAM-SIT and HiRAM-SIT underestimate the SST, whereas ECHAM5-SIT

327   overestimates the SST. Warm SST bias in the eastern tropical Pacific was simulated in

328   the three models because of the lack of oceanic circulation in the SIT. The simulated zonal

329   wind in the three models (Fig. S6b–d) demonstrated different responses to coupling.

330   Figure S6c, d presents the 850 hPa zonal wind differences between coupled and

331   uncoupled models (shading) and the total field in uncoupled models (contours). Figure

332   S6f–h shows the 10°S–EQ averaged 850 hPa zonal in both coupled and uncoupled models.

333   In ECHAM5-SIT, the westerly wind is slightly enhanced in the eastern Indian Ocean but

334   decreases in the western Indian Ocean and western Pacific. In CAM5-SIT, westerly wind

335   reduces in the Indian Ocean but enhances over the western Pacific. The HiRAM-SIT has

336   similar changes as in ECHAM5-SIT, with decreases over the Maritime Continent area

337   but increases in the western Indian Ocean and Pacific. In general, the three models

338   disagree in the changes in zonal wind mean state in response to coupling.

339   The mean moisture changes are substantially enhanced over the tropical areas in

340   ECHAM5 after coupling (Fig. S7b, e). However, in both CAM5 and HiRAM, no clear

341   change was observed to the south, but strong drying was observed to the north of equator

342   (Fig. S7c, d, f, g). The only common feature among the three models that is enhanced in

343   the coupled simulations is the meridional gradient of mean moisture. This is consistent

344   with many previous studies (Kim et al. 2014; Jiang et al. 2018; Ahn et al. 2020). Our

345   budget analysis indicated that the meridional transport by the intraseasonal meridional

Geoscientific
Model Development
Discussions

346   circulation is the dominant term, and the meridional gradient of mean moisture is the

347   secondary effect in enhancing MJO simulations by coupling. The mean precipitation

348   changes are more consistent among the three models after coupling (Fig. S8). One of the

349   major changes is the southward shift of the major precipitation zone, resulting in

350   precipitation increases over the regions south of the equator except in the Maritime

351   Continent. Similarly, the precipitation intraseasonal variance (20–100 days filtered)

352   markedly enhances in these regions (Fig. S9). The ECHAM5-SIT exhibits a relatively

353   minor increase over the western Maritime Continent. By contrast, the HiRAM-SIT

354   exhibits the strongest enhancement, particularly in the Indian Ocean. In general, all three

355   coupled models enhance the intraseasonal signals over the tropics with discrepancies in

356   detail. By contrast, the model mean state does not substantially improve after coupling.

357   Thus, in this study, the mean state is not the main contribution to the enhancement of the

358   MJO simulation after coupling. Instead, coupling leading to rigorous atmosphere–ocean

359   interaction is likely the reason for the improvement of MJO simulation.

360

361   **3.4 The forecast model: CWBGFS**

362   CWBGFS and CWBGFS-SIT were compared for only 3 years. Figure 11

363   demonstrates the wave number–frequency spectra and the 10°S–10°N averaged lag–

364   longitude diagrams of CWBGFS between coupled and uncoupled versions. The spectra

365   of CWBGFS-SIT suggest better simulation (Fig. 11a, b) in relation to better propagation

366   across the MC (Fig. 11c, d). Although we did not examine the mechanisms in detail, our

367   results demonstrate that MJO forecast skills could be improved by considering the

368   coupling effect in the forecast model.

18

4 Discussion

This study used a one-column TKE-type ocean mixed-layer model SIT coupled with AGCMs to improve MJO simulation. SIT is designed to have fine layers near the surface and can simulate their warm layer, cool skin, and diurnal fluctuations. This refined discretization under the ocean surface in SIT provides improved SST simulation and, thus, realistic air–sea interaction. Coupling SIT with ECHAM5, CAM5, and HiRAM significantly improves the MJO simulation in the three AGCMs compared with that in prescribed SST-driven AGCMs. The vertical cross section indicates that the strengthened low-level convergence during the preconditioning phase is better simulated in the coupled experiment. Furthermore, the phase variation and amplitude of the SST and ocean temperature under the surface can be realistically simulated. Our results reveal that the MJO can be realistically simulated in terms of strength, period, and propagation speed by increasing the vertical resolution of the one-column ocean model to better resolve the upper-ocean warm layer.

The MSE budget analysis revealed that the coupling effects during the earlier phases and mature phase exhibit different contributions. During the preconditioning phase, the positive contribution of vertical advection and negative contribution of LH in MSE tendency are closer to realistic values in coupled simulations during the initial phase of the MJO. During the mature phase of the strongest convection in the MC, the meridional component of the horizontal advection term is the dominant term to enhance the simulation after coupling. Improved meridional circulation is essential in the coupled simulations that outperformed uncoupled experiments. The results confirm that the dominance of dynamic influence over thermodynamic influence in response to the

392   atmosphere–ocean coupling is the key process leading to the improvement of MJO

393   simulations.

394   In summary, this study suggests two major enhancements of the coupling process.

395   First, during the preconditioning phase of the MJO over MC, the underestimated surface

396   LH bias in AGCMs can be corrected. Second, during the strongest convection phase over

397   MC, the change in intraseasonal circulation in the meridional circulation is the dominant

398   factor in coupled simulations relative to uncoupled experiments. Although many studies

399   have indicated the key role played by the mean state, the mean state in our simulations

400   provides only a secondary contribution to enhancing MJO simulation, with coupling

401   being the main contributor. For example, zonal wind and precipitation changed

402   inconsistently among the three models after coupling. Instead, the meridional gradient of

403   the mean moisture and intraseasonal variance of precipitation have a better relationship

404   after coupling. Therefore, coupling leading to rigorous atmosphere–ocean interaction, but

405   not change in mean states, is likely the reason for MJO simulation improvement.

406   Moreover, coupling SIT with the weather forecast model CWBCFS can improve MJO.

407   This study supports previous findings (Tseng et al. 2015) that the enhancement of

408   atmosphere–ocean coupling by considering extremely high vertical resolution in the first

409   few meters of the ocean model improves MJO simulations, and this improvement is

410   independent of AGCMs with different configurations and physical parameterization

411   schemes. Resolving the atmosphere–ocean coupling may be more beneficial than

412   modifying the atmospheric physical parameterization schemes in GCM.

413

414 **Code and data availability.** The model code of CAM5 – SIT, ECHAM5-SIT and

415 HiRAM-SIT is available at https://doi.org/10.5281/zenodo.5701538,

416 https://doi.org/10.5281/zenodo.5510795 and https://doi.org/10.5281/zenodo.5701579.

417 Observational data used in this study include precipitation from Global

418 Precipitation Climatology Project V1.3 (GPCP, 1° resolution), outgoing longwave

419 radiation (OLR, 1° resolution), and daily SST (Optimum Interpolated SST, 0.25°

420 resolution) from the National Oceanic and Atmosphere Administration, and variables

421 were obtained from the European Centre for Medium-range Weather Forecast

422 Reanalysis-interim. All model codes and data availability presented here can be obtained

423 by contacting the first author, Dr. Wan-Ling Tseng (wtseng@gate.sinica.edu.tw).

424

425 **Author contributions.** HHH and WLT have responsibility for conceptualization,

426 including analyzing the data and writing the manuscript. YYL, PHK, BJT, CYT and HCL

427 developed the model and provided the simulations.

428

429 **Competing interests.** The authors declare that they have no conflict of interest.

430

438

References

Adler, R. F., and Coauthors, 2003: The version-2 global precipitation climatology
    project (GPCP) monthly precipitation analysis (1979-present). *Journal of
    Hydrometeorology*, **4,** 1147-1167.

Ahn, M. S., and Coauthors, 2020: MJO propagation across the Maritime Continent: Are
    CMIP6 models better than CMIP5 models? *Geophysical Research Letters*, **47,**
    e2020GL087250.

Banzon, V. F., R. W. Reynolds, D. Stokes, and Y. Xue, 2014: A 1/4-spatial-resolution
    daily sea surface temperature climatology based on a blended satellite and in situ
    analysis. *Journal of Climate*, **27,** 8221-8228.

Behringer, D., and Y. Xue, 2004: Evaluation of the global ocean data assimilation
    system at NCEP: The Pacific Ocean. *Proc. Eighth Symp. on Integrated Observing
    and Assimilation Systems for Atmosphere, Oceans, and Land Surface*.

Benedict, J. J., and D. A. Randall, 2011: Impacts of Idealized Air–Sea Coupling on
    Madden–Julian Oscillation Structure in the Superparameterized CAM. *Journal of
    the Atmospheric Sciences*, **68,** 1990-2008.

Chen, C.-A., H.-H. Hsu, C.-C. Hong, P.-G. Chiu, C.-Y. Tu, S.-J. Lin, and A. Kitoh,
    2019: Seasonal precipitation change in the western North Pacific and East Asia
    under global warming in two high-resolution AGCMs. *Climate Dynamics*, **53,**
    5583-5605.

Chi, N. H., R. C. Lien, E. A. D'Asaro, and B. B. Ma, 2014: The surface mixed layer heat
    budget from mooring observations in the central Indian Ocean during Madden–
    Julian Oscillation events. *Journal of Geophysical Research: Oceans*, **119,** 4638-
    4652.

463   CLIVAR, M. J. O. W. G., 2009: MJO Simulation Diagnostics. *Journal of Climate*, **22,**

464   3006-3030.

465   Dee, D., and Coauthors, 2011: The ERA-Interim reanalysis: Configuration and

466   performance of the data assimilation system. *Quarterly Journal of the Royal*

467   *Meteorological Society*, **137,** 553-597.

468   Del Genio, A. D., and Y. Chen, 2015: Cloud-radiative driving of the Madden-Julian

469   oscillation as seen by the A-Train. *Journal of Geophysical Research: Atmospheres*,

470   **120,** 5344-5356.

471   DeMott, C. A., N. P. Klingaman, and S. J. Woolnough, 2015: Atmosphere-ocean

472   coupled processes in the Madden-Julian oscillation. *Reviews of Geophysics*, **53,**

473   1099-1154.

474   DeMott, C. A., J. J. Benedict, N. P. Klingaman, S. J. Woolnough, and D. A. Randall,

475   2016: Diagnosing ocean feedbacks to the MJO: SST-modulated surface fluxes and

476   the moist static energy budget. *Journal of Geophysical Research: Atmospheres*,

477   **121,** 8350-8373.

478   DeMott, C. A., N. P. Klingaman, W. L. Tseng, M. A. Burt, Y. Gao, and D. A. Randall,

479   2019: The convection connection: How ocean feedbacks affect tropical mean

480   moisture and MJO propagation. *Journal of Geophysical Research: Atmospheres*,

481   **124,** 11910-11931.

482   Drushka, K., J. Sprintall, S. T. Gille, and S. Wijffels, 2012: In situ observations of

483   Madden-Julian Oscillation mixed layer dynamics in the Indian and western Pacific

484   Oceans. *Journal of Climate*, **25,** 2306-2328.

485   Duchon, C. E., 1979: Lanczos filtering in one and two dimensions. *Journal of Applied*

486   *Meteorology and Climatology*, **18,** 1016-1022.

487   Flatau, M., P. J. Flatau, P. Phoebus, and P. P. Niiler, 1997: The feedback between

488   equatorial convection and local radiative and evaporative processes: The

489   implications for intraseasonal oscillations. *Journal of the atmospheric sciences*, **54,**

490   2373-2386.

491   Fu, X., and Coauthors, 2015: Distinctive roles of air–sea coupling on different MJO

492   events: A new perspective revealed from the DYNAMO/CINDY field campaign.

493   *Monthly Weather Review*, **143,** 794-812.

494   Gaspar, P., Y. Gregoris, and J.-M. Lefevre, 1990: A simple eddy kinetic energy model

495   for simulations of the oceanic vertical mixing: Tests at station Papa and long-term

496   upper ocean study site. *Journal of Geophysical Research: Oceans*, **95,** 16179-

497   16193.

498   Hendon, H. H., and M. L. Salby, 1994: The life cycle of the Madden-Julian oscillation.

499   *Journal of the Atmospheric Sciences*, **51,** 2225-2237.

500   Hendon, H. H., B. Liebmann, and J. D. Glick, 1998: Oceanic Kelvin waves and the

501   Madden–Julian oscillation. *Journal of the Atmospheric Sciences*, **55,** 88-101.

502   Hong, S.-Y., and H.-L. Pan, 1996: Nonlocal boundary layer vertical diffusion in a

503   medium-range forecast model. *Monthly weather review*, **124,** 2322-2339.

504   Hsu, P.-C., and T. Li, 2012: Role of the Boundary Layer Moisture Asymmetry in

505   Causing the Eastward Propagation of the Madden-Julian Oscillation*. *Journal of

506   Climate*, **25,** 4914-4931.

507   Hurrell, J. W., and Coauthors, 2013: The community earth system model: a framework

508   for collaborative research. *Bulletin of the American Meteorological Society*, **94,**

509   1339-1360.

510   Inness, P. M., J. M. Slingo, E. Guilyardi, and J. Cole, 2003: Simulation of the Madden-

511   Julian Oscillation in a coupled general circulation model. Part II: The role of the

512   basic state. *Journal of Climate*, **16,** 365-382.

513   Jiang, X., Á. F. Adames, M. Zhao, D. Waliser, and E. Maloney, 2018: A unified

514   moisture mode framework for seasonality of the Madden–Julian oscillation.

515   *Journal of Climate*, **31,** 4215-4224.

516   Jiang, X., and Coauthors, 2020: Fifty years of research on the Madden-Julian

517   Oscillation: Recent progress, challenges, and perspectives. *Journal of Geophysical*

518   *Research: Atmospheres*, **125,** e2019JD030911.

519   Kang, I.-S., F. Liu, M.-S. Ahn, Y.-M. Yang, and B. Wang, 2013: The Role of SST

520   Structure in Convectively Coupled Kelvin-Rossby Waves and Its Implications for

521   MJO Formation. *Journal of Climate*, **26,** 5915–5930.

522   Kim, D., A. H. Sobel, E. D. Maloney, D. M. Frierson, and I.-S. Kang, 2011: A

523   systematic relationship between intraseasonal variability and mean state bias in

524   AGCM simulations. *Journal of Climate*, **24,** 5506-5520.

525   Kim, D., and Coauthors, 2009: Application of MJO simulation diagnostics to climate

526   models. *Journal of climate*, **22,** 6413-6436.

527   Kim, H.-M., P. J. Webster, V. E. Toma, and D. Kim, 2014: Predictability and prediction

528   skill of the MJO in two operational forecasting systems. *Journal of Climate*, **27,**

529   5364-5378.

530   Klingaman, N., and S. Woolnough, 2013: The role of air–sea coupling in the simulation

531   of the Madden–Julian oscillation in the Hadley Centre model. *Quarterly Journal of*

532   *the Royal Meteorological Society*.

533   Klingaman, N. P., and C. A. Demott, 2020: Mean state biases and interannual variability

534   affect perceived sensitivities of the Madden-Julian Oscillation to air-sea coupling.

535   *Journal of Advances in Modeling Earth Systems*, **12,** e2019MS001799.

536   Krishnamurti, T. N., D. Oosterhof, and A. Mehta, 1988: Air–sea interaction on the time

537   scale of 30 to 50 days. *Journal of the atmospheric sciences*, **45,** 1304-1322.

538   Li, C. W., and J. Wang, 2000: Large eddy simulation of free surface shallow-water

539   flow. *International journal for numerical methods in fluids*, **34,** 31-46.

540   Li, Y., and R. E. Carbone, 2012: Excitation of Rainfall over the Tropical Western

541   Pacific. *Journal of the Atmospheric Sciences*, **69,** 2983-2994.

542   Liebmann, B., 1996: Description of a complete (interpolated) outgoing longwave

543   radiation dataset. *Bull. Amer. Meteor. Soc.*, **77,** 1275-1277.

544   Liou, C. S., and Coauthors, 1997: The second–generation global forecast system at the

545   central weather bureau in Taiwan. *Weather and Forecasting*, **12,** 653-663.

546   Madden, R. A., and P. R. Julian, 1972: Description of global-scale circulation cells in

547   the tropics with a 40-50 day period. *J. atmos. Sci*, **29,** 1109-1123.

548   Marshall, A. G., O. Alves, and H. H. Hendon, 2008: An Enhanced Moisture

549   Convergence–Evaporation Feedback Mechanism for MJO Air–Sea Interaction.

550   *Journal of the Atmospheric Sciences*, **65,** 970-986.

551   Matthews, A. J., P. Singhruck, and K. J. Heywood, 2007: Deep ocean impact of a

552   Madden-Julian Oscillation observed by Argo floats. *Science*, **318,** 1765-1769.

553   McPhaden, M. J., A. J. Busalacchi, and D. L. Anderson, 2010: A toga retrospective.

554   *Oceanography*, **23,** 86-103.

555   Nordeng, T. E., 1994: *Extended versions of the convective parametrization scheme at*

556   *ECMWF and their impact on the mean and transient activity of the model in the*

557   *tropics.* European Centre for Medium-Range Weather Forecasts.

558   Oliver, E., and K. Thompson, 2011: Sea level and circulation variability of the Gulf of

559   Carpentaria: Influence of the Madden-Julian Oscillation and the adjacent deep

560   ocean. *Journal of Geophysical Research: Oceans*, **116**.

561   Roeckner, E., 2003: *The atmospheric general circulation model ECHAM5: Part 1:*

562   *model description.* Max-Planck-Institut fuer Meteorologie.

563   Roeckner, E., and Coauthors, 2006: Sensitivity of simulated climate to horizontal and

564   vertical resolution in the ECHAM5 atmosphere model. *Journal of Climate*, **19,**

565   3771-3791.

566   Salby, M. L., and H. H. Hendon, 1994: Intraseasonal behavior of clouds, temperature,

567   and motion in the tropics. *Journal of the Atmospheric Sciences*, **51,** 2207-2224.

568   Shinoda, T., and H. H. Hendon, 1998: Mixed layer modeling of intraseasonal variability

569   in the tropical western Pacific and Indian Oceans. *Journal of Climate*, **11,** 2668-

570   2685.

571   Shinoda, T., H. H. Hendon, and J. Glick, 1998: Intraseasonal variability of surface

572   fluxes and sea surface temperature in the tropical western Pacific and Indian

573   Oceans. *Journal of climate*, **11,** 1685-1702.

574   Sobel, A. H., E. D. Maloney, G. Bellon, and D. M. Frierson, 2008: The role of surface

575   heat fluxes in tropical intraseasonal oscillations. *Nature Geoscience*, **1,** 653-657.

576   ——, 2010: Surface fluxes and tropical intraseasonal variability: A reassessment.

577   *Journal of Advances in Modeling Earth Systems*, **2**.

578   Team, G. G. A. M. D., and Coauthors, 2004: The new GFDL global atmosphere and

579   land model AM2–LM2: Evaluation with prescribed SST simulations. *Journal of*

580   *Climate*, **17,** 4641-4673.

581   Tseng, W.-L., B.-J. Tsuang, N. Keenlyside, H.-H. Hsu, and C.-Y. Tu, 2015: Resolving

582   the upper-ocean warm layer improves the simulation of the Madden–Julian

583   oscillation. *Climate Dynamics*, 1-17.

584   Tsuang, B.-J., C.-Y. Tu, J.-L. Tsai, J. A. Dracup, K. Arpe, and T. Meyers, 2009: A more

585   accurate scheme for calculating Earths-skin temperature. *Climate Dynamics*, **32,**

586   251-272.

587   Tu, C.-Y., and B.-J. Tsuang, 2005: Cool-skin simulation by a one-column ocean model.

588   *Geophysical research letters*, **32**.

589   Wang, B., and H. Rui, 1990: Dynamics of the Coupled Moist Kelvin-Rossby Wave on

590   an Equatorial-Plane. *Journal of the Atmospheric Sciences*, **47,** 397-413.

591   Wang, B., and X. Xie, 1998: Coupled modes of the warm pool climate system. Part I:

592   The role of air–sea interaction in maintaining Madden–Julian oscillation. *Journal*

593   *of Climate*, **11,** 2116-2135.

594   Wang, G., Z. Ling, R. Wu, and C. Chen, 2013: Impacts of the Madden–Julian

595   oscillation on the summer South China Sea ocean circulation and temperature.

596   *Journal of climate*, **26,** 8084-8096.

597   Wang, Y.-C., W.-L. Tseng, and H.-H. Hsu, 2021: Role of Convection–circulation

598   Coupling in the Propagation Mechanism of the Madden–Julian Oscillation over the

599   Maritime Continent in Climate Models.

600   Watterson, I., and J. Syktus, 2007: The influence of air–sea interaction on the Madden–

601   Julian oscillation: The role of the seasonal mean state. *Climate dynamics*, **28,** 703-

602   722.

603   Webber, B. G., A. J. Matthews, and K. J. Heywood, 2010: A dynamical ocean feedback

604   mechanism for the Madden–Julian oscillation. *Quarterly Journal of the Royal*

605   *Meteorological Society: A journal of the atmospheric sciences, applied*

606   *meteorology and physical oceanography*, **136,** 740-754.

607   Webber, B. G., A. J. Matthews, K. J. Heywood, and D. P. Stevens, 2012: Ocean Rossby

608   waves as a triggering mechanism for primary Madden–Julian events. *Quarterly*

609   *Journal of the Royal Meteorological Society*, **138,** 514-527.

610   Wheeler, M. C., and H. H. Hendon, 2004: An all-season real-time multivariate MJO

611   index: Development of an index for monitoring and prediction. *Monthly Weather*

612   *Review*, **132,** 1917-1932.

613   Woolnough, S. J., J. M. Slingo, and B. J. Hoskins, 2000: The relationship between

614   convection and sea surface temperature on intraseasonal timescales. *Journal of*

615   *Climate*, **13,** 2086-2104.

616   Yanai, M., S. Esbensen, and J.-H. Chu, 1973: Determination of bulk properties of

617   tropical cloud clusters from large-scale heat and moisture budgets. *Journal of the*

618   *Atmospheric Sciences*, **30,** 611-627.

619   Zhang, C., 2005: Madden-Julian oscillation. *Reviews of Geophysics*, **43**.

620   Zhao, M., I. M. Held, S.-J. Lin, and G. A. Vecchi, 2009: Simulations of global hurricane

621   climatology, interannual variability, and response to global warming using a 50-km

622   resolution GCM. *Journal of Climate*, **22,** 6653-6678.

623

29

		ECHAM5-SIT	CAM5-SIT	HiRAM-SIT	CWBGFS-SIT
AGCM		ECHAM5	CAM5	HiRAM	CWBGFS
Horizontal resolution		T63(~2°)	1.9°X2.5°	1°X1°	T319
BC	SST	OISST	OISST	OISST	OISST
	SIC	OISST	OISST	OISST	OISST
	OT/OS	GODAS	GODAS	GODAS	GODAS
Atmosphere vertical resolution		L31	L30	L32	L60
Ocean vertical resolution		42	42	42	42
Coupled region		30˚S-30˚N	30˚S-30˚N	30˚S-30˚N	30˚S-30˚N,30˚-40˚, blending interpolated
Time		1985-2005 (21 years)			2012-2014 (3 years)

624
625 **Table 1.** Detailed information of models and experiments.

626

30

627
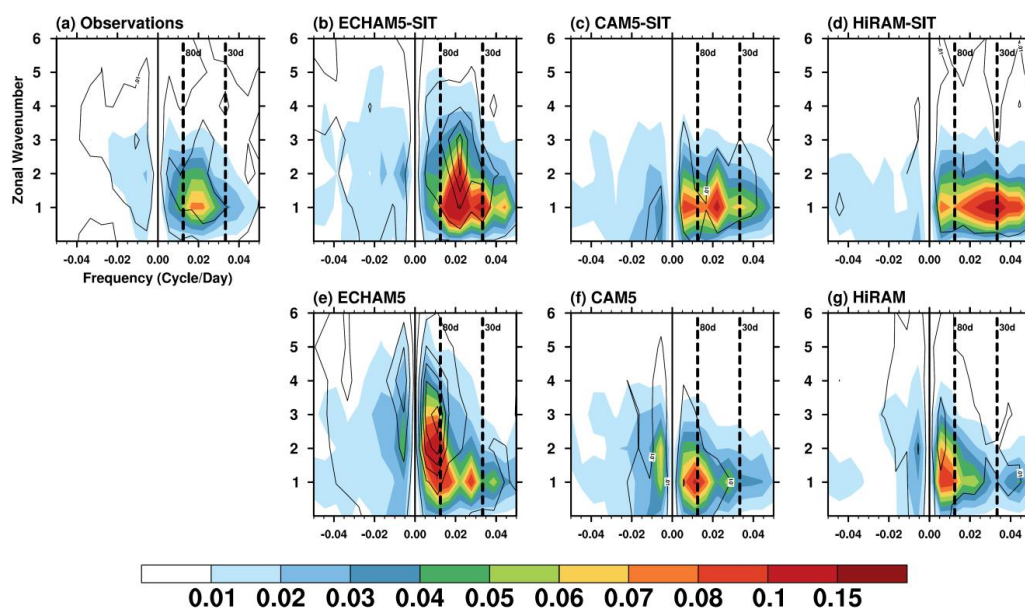
Figure 1. Wave number–frequency spectra for equatorial 850 hPa zonal wind (shading)

and precipitation (contours) over 10°S–10°N from (a) observations and simulations by

using the (b–d) coupled and (e–g) uncoupled AGCM.

633

634
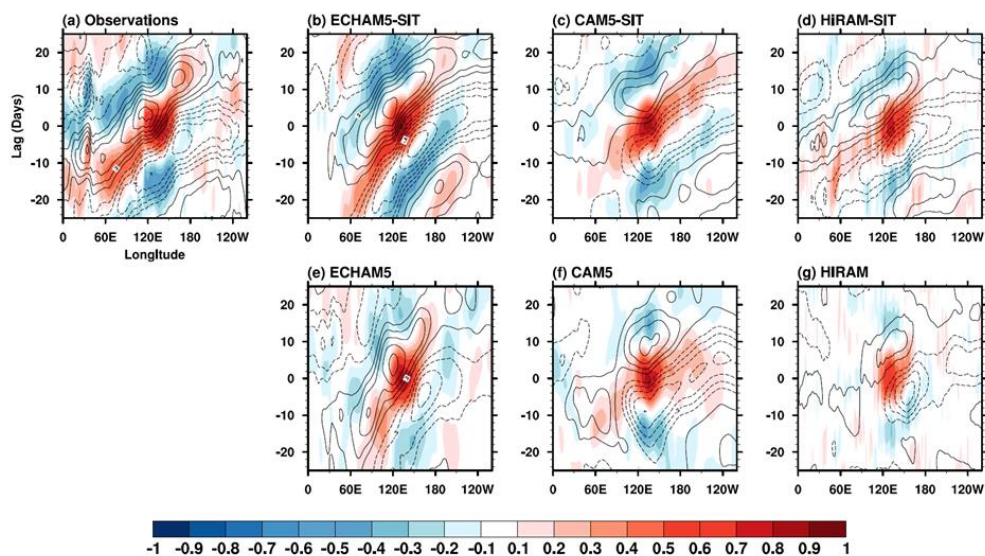
Figure 2. The 10°S–10°N averaged lag–longitude diagrams of intraseasonal precipitation

(shading) and 10-m zonal wind (contour) correlated against precipitation at region (10°S–

5°N, 120°E–150°E) from (a) observations and simulations by using the (b–d) coupled

and (e–g) uncoupled AGCM. The contour interval is 0.1.

639

640
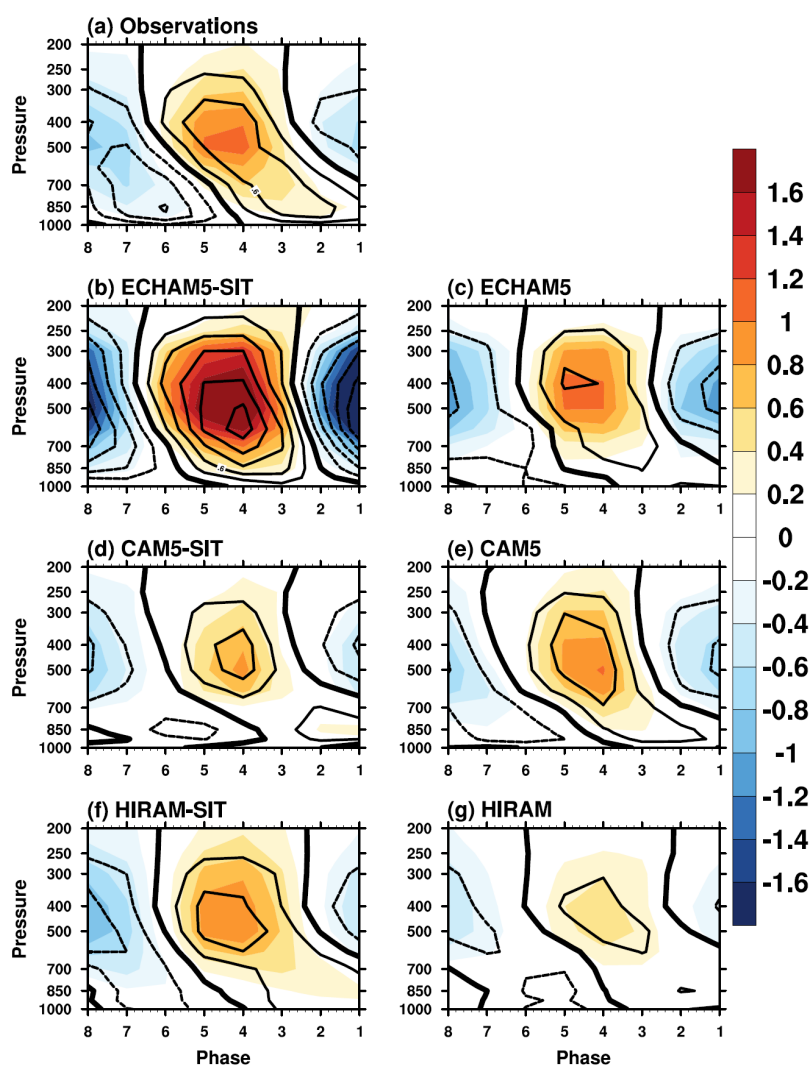
Figure 3. Vertical profiles with respect to MJO phases averaged over 10°S–EQ and
120°E–150°E for intraseasonal anomalies (i.e., with 20–100-day filtering) of Q1 (shading;
K day^{-1}) and Q2 (contours; K day^{-1}) from (a) observations and simulations by using the
(b–d) coupled and (e–g) uncoupled AGCM.

Geoscientific
Model Development
Discussions
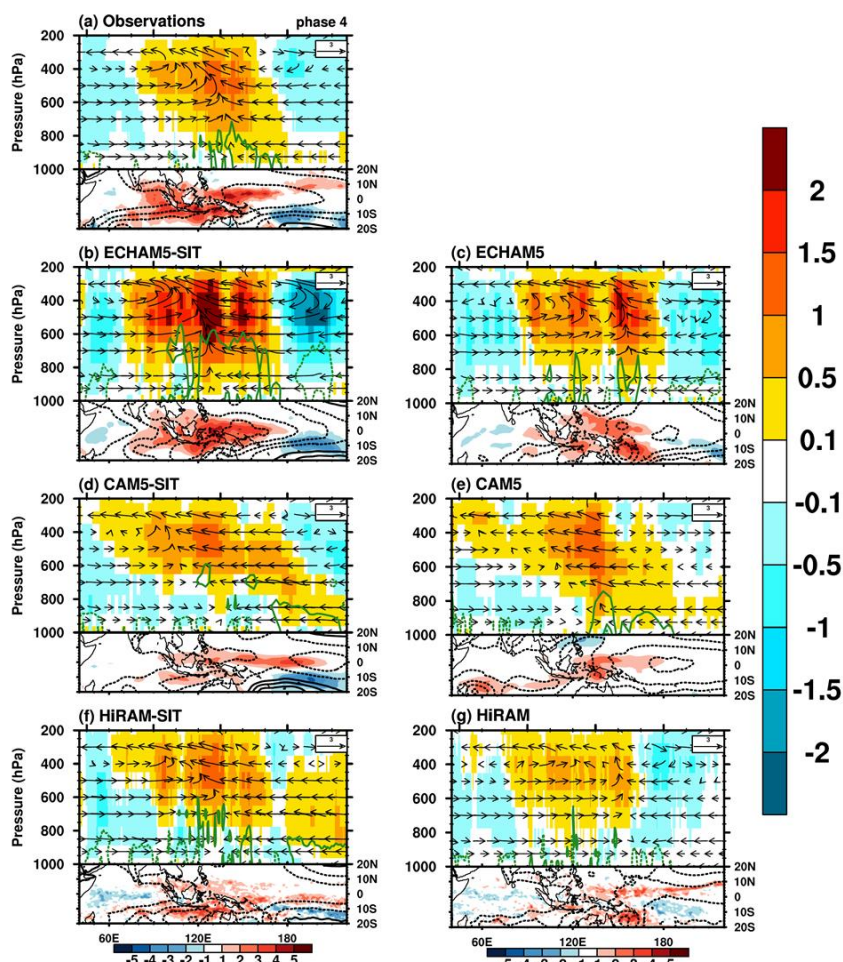
Figure 4. Structure of simulated MJO in phase 4. The longitude–height cross-sections (averaged over 10°S–EQ) of the MJO scaled wind circulation (vector, u: m s^{-1}, omega: 10^{-2} Pa s^{-1}), Q1 (shading, unit: K day^{-1}), and the horizontal moisture convergence (green contour, unit: 10^{-6} g kg^{-1} s^{-1}) from (a) observations and simulations by using the (b–d) coupled and (e–g) uncoupled AGCM. The contour interval of the moisture convergence is 8 × 10^{-6} g kg^{-1} s^{-1}; solid line is positive. Precipitation (shading, unit: mm day^{-1}) and sea

654   level pressure (contour, unit: hPa). Contour interval of sea level pressure is 30 hPa; dashed

655   line indicates negative.

656
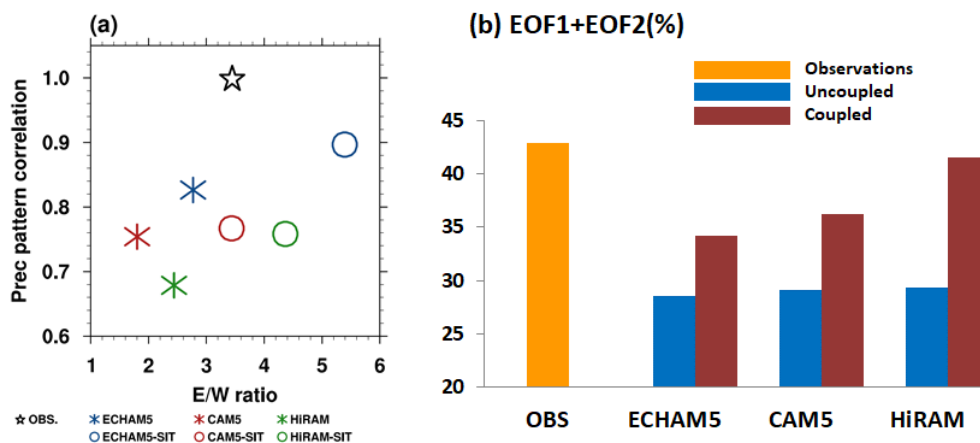
Figure 5. Scatter plots of various MJO indices based on observation and experiments (Table 1). (a) X-axis is the power ratio of east–west propagating waves. The east–west ratio was calculated through the division of the sum of eastward-propagating power by the westward-propagating counterpart within wavenumbers 1–3 (1–2 for zonal wind), period 30–80 days. The Y-axis is the pattern correlation of precipitation eastward propagation, as shown in Fig. 2. (b) Sum of RMM1 and RMM2 variances based on Wheeler and Hendon (2004).

36
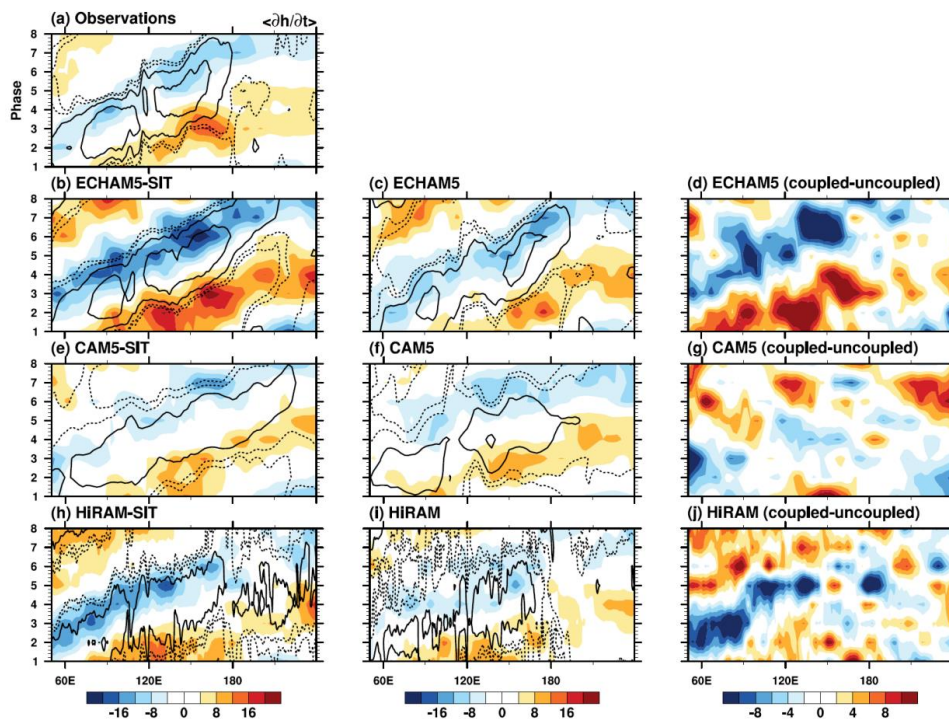
Figure 6. The 10°S–EQ averaged Hovmöller diagrams of MSE (shading) and precipitation (contour) composite followed the RMM index from (a) observations and simulations by using the (b, e, j) coupled and (c, f, k) uncoupled AGCM and (d, i, l) their difference. The contour interval is precipitation anomalies.
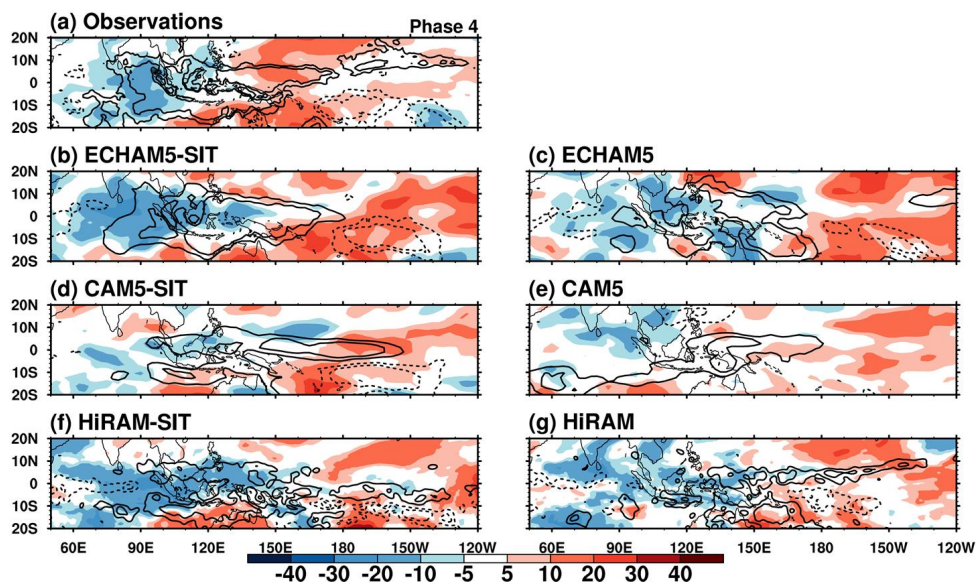
37
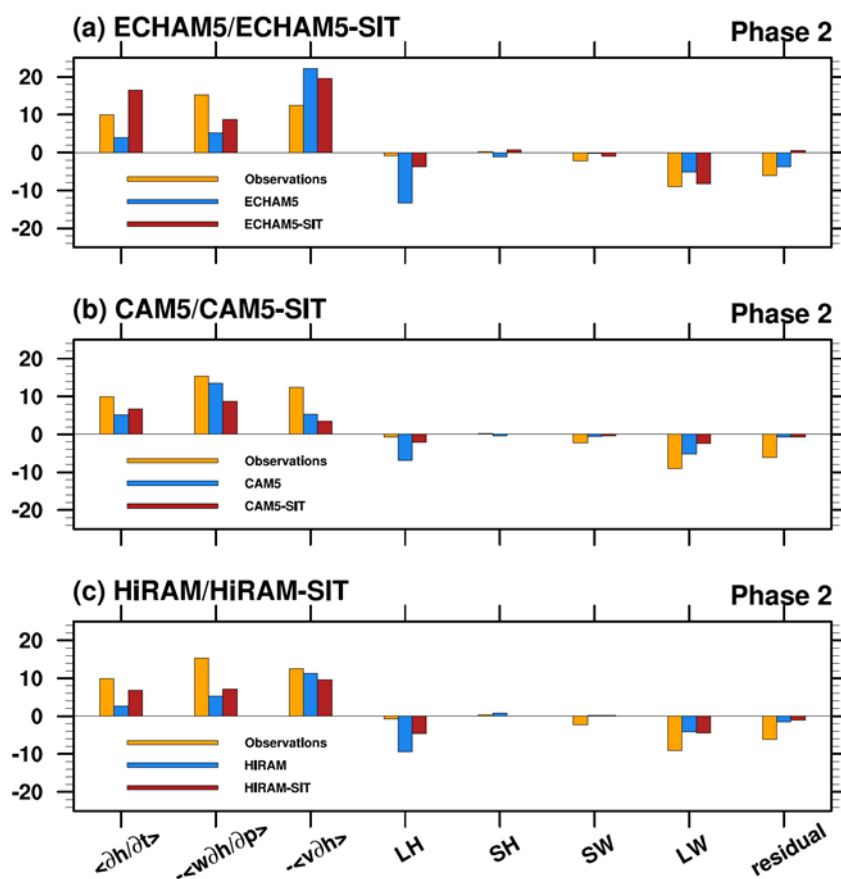
Figure 7. Model-simulated column-integrated MSE budget terms (J kg^{-1} s^{-1}) during phase 2 of the MJO. Data from the observations, Nordeng scheme simulation, and Tiedtke scheme simulation are shown in black, red, and blue, respectively. The averaged domain is 10°S–EQ and 120°–150°E.
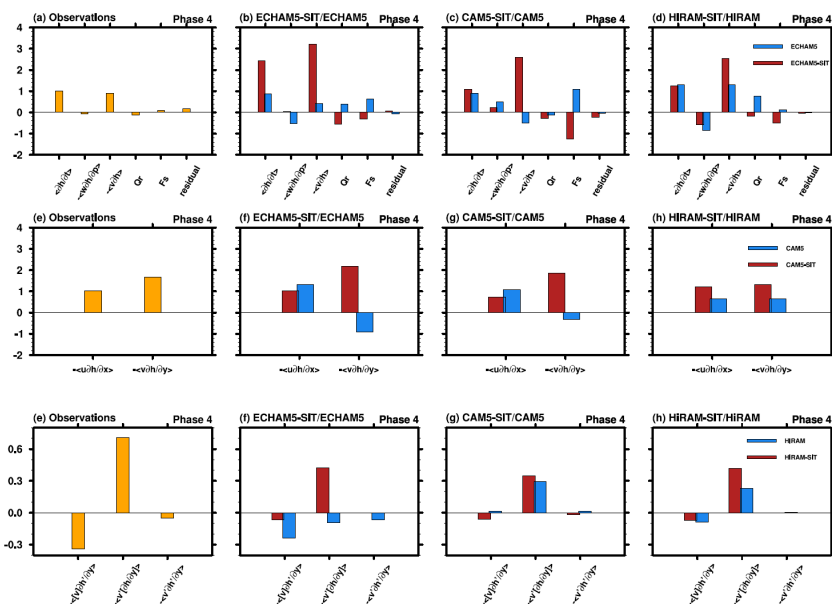
680

681

Figure 8. Phase 4 of the column-integrated MSE tendency (shading) and precipitation

(contours) based on (a) observation, (b) ECHAM5-SIT, (c) ECHAM5, (d) CAM5-SIT,

(e) CAM5, (g) HiRAM-SIT, and (f) HiRAM. The nine-point local smoothing is applied

in the intraseasonal precipitation variance of HiRAM here (contours only).

686

687

39

688

689

Figure 9. (a–d) Relative role of each MSE component of phase 4 through the projection of the spatial pattern of each MSE budget over the MC (domain) onto the total MSE tendency pattern (Fig. 8a). (e–h) Decomposite of the total horizontal MSE advection based on zonal and meridional components. (i–l) Decomposite of the meridional horizontal MSE advection based on the MJO circulation and the mean state of moisture.
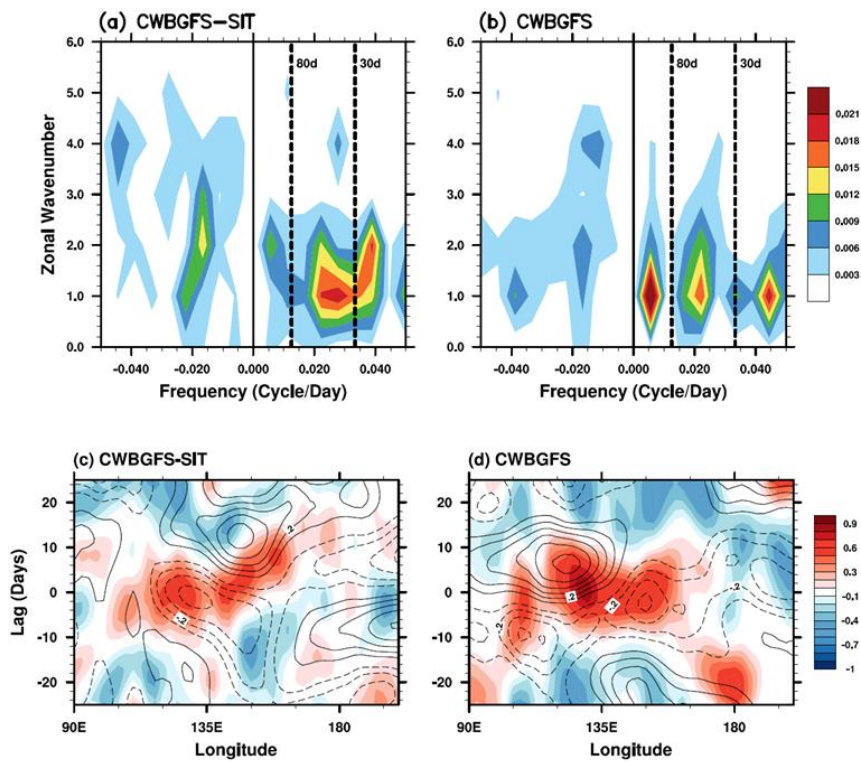
695
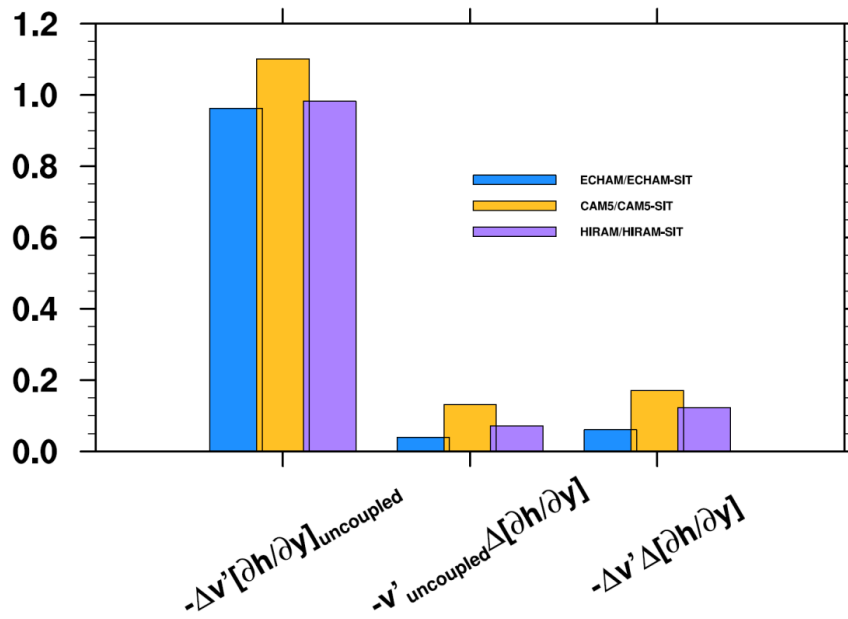
Figure 10. Bar chart of relative contribution of intraseasonal convergence and background moisture between the coupled and uncoupled change in MJO phase 4.

41

701

Figure 11. (a, b) Same as Fig. 1, but in CWBGFS-SIT and CWBGFS. (c, d) Same as Fig.

2, but in CWBGFS-SIT and CWBGFS.

704

705